Citation for final published version:

Zhang, Shi, Dedovets, Dmytro, Feng, Andong, Wang, Kang and Pera Titus, Marc 2022. Pickering interfacial catalysis for aerobic alcohol oxidation in oil foams. Journal of the American Chemical Society 144 (4) , 1729–1738. 10.1021/jacs.1c11207

Publishers page: http://dx.doi.org/10.1021/jacs.1c11207

Pickering Interfacial Catalysis for Aerobic Alcohol Oxidation in Oil Foams

Shi Zhang, Dmytro Dedovets, Andong Feng, Kang Wang, and Marc Pera-Titus*

ACCESS | Metrics & More | Article Recommendations | * Supporting Information

ABSTRACT: Oil foams stabilized by surface-active catalytic particles bearing fluorinated chains and Pd nanoparticles allowed fast and efficient aerobic oxidation of a variety of aromatic and aliphatic alcohols compared to bulk catalytic systems at ambient O_2 pressure. High foam stability was achieved at low particle concentration (<1 wt %) provided that the contact angle locates in the range 41°−73°. The catalytic performance was strongly affected by the foaming properties, with 7−10 times activity increase in pure O_2 compared to nonfoam systems. Intermediate foam stability was required to achieve good catalytic activity, combining large interfacial area and high gas exchange rate. Particles were conveniently recycled with high foamability and catalytic efficiency maintained for at least seven consecutive runs.

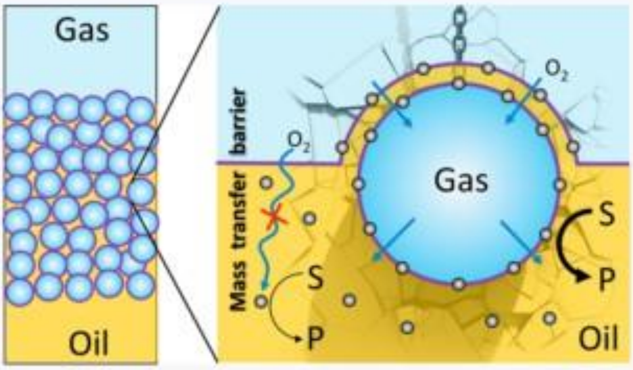

1. INTRODUCTION

Gas−liquid−solid (G−L−S) reactions are ubiquitous in chemical, petrochemical, biochemical, and environmental catalytic processes. Conventional reactors such as packed beds (e.g., trickle beds and bubble columns) and stirred reactors typically suffer from low gas solubility in liquids and resilient mass/heat transfer limitations, especially when dealing with fast reactions.[1] In practice, cosolvents, surfactants, G−L phase-transfer reagents (e.g., molten salts), and high gas pressures can be employed to promote the G−L contact and increase the gas concentration at the expense of the green footprint of the process. Also, continuous flow microreactors[2] and catalytic membrane reactors[3] have been advocated for increasing the G−L interfacial area. However, these systems require complex equipment and still do not guarantee an efficient L−S contact on the catalyst surface. For a major improvement in terms of cost efficiency and energy savings, G−L−S reactors operating at the nanoscale are required.

This approach was demonstrated with Pickering emulsions, which can be used to engineer catalytic reactions between two immiscible liquid reagents, affording an intimate contact between the phases and facile product separation.[4] Despite this significant progress, the transposition of Pickering emulsions to G−L systems based on "armored" bubbles (e.g., foams) has been seldom explored.[5] Yuan and co-workers synthesized particles based on monodisperse Au nanoparticles embedded in $[PV_2Mo_{10}O_{40}]^{5-}$ assembled to 1,3,5-tris[(3-methylimidazolium)methyl]-2,4,6-trimethylbenzene tribromide by electrostatic interactions.[6] The particles could self-assemble at the O_2/water interface, stabilizing O_2 microbubbles which show high activity in the oxidation of aliphatic/aromatic alcohols into aldehydes and ketones. Yang and co-workers synthesized silica particles modified with octyl and polyamine groups stabilizing gas microbubbles in water.[7] By incorporation of Pd or Au nanoparticles, the particles became active for aqueous hydrogenation and oxidation reactions in H_2 and O_2 foams, respectively, under stirring at high particle concentration (7.5−12.5 wt %). The catalytic foams exhibited an enhanced activity compared to conventional multiphasic reactors, where the catalyst is dispersed within the continuous phase. These studies are limited to aqueous systems only, whereas catalytic reactions often require organic solvents.

Aqueous foams and "armored bubbles" can be stabilized by a variety of particles, including hydrophobic silicas,[8] polymers,[9] cellulose,[10] and surfactant crystals.[11] In contrast, only few reports are available on particle-stabilized nonaqueous foams, consisting of low-surface-energy fluoropolymers/oligomers,[12] particles bearing fluorocarbon chains,[13] and highly hydrophobic low-carbon chains.[14] This limited scope arises from the low surface tension of organic liquids, restricting particle adsorption at the G−L interface.[15] Besides, particle-stabilized foams differ from emulsions by a significant difference in density between the phases, which is similar for L−L systems but can vary orders of magnitude for G−L systems. As a

Table 1. Main Properties of Catalytic Particles

catalyst	Pd (wt %)[a]	F (wt %)[b]	D_{silica} (nm)[c]	D_{Pd} (nm)[c]	contact angle (deg)[d]	
					xylene	BnOH
Pd@SiNP_F_{17}(1−4)	1.33	33	364	3.6	53.9	95.9
Pd@SiNP_F_{17}(1−8)	1.49	25	289	6.8	30.3	69.9
Pd@SiNP_F_{17}(1−16)	1.78	15	304	5.1	11.7	53.2
Pd@SiNP_C_8(1−4)	0.82		244	2.9	<10	27.3

[a]Measured by ICP-OES.[b] Measured by TGA.[c]Measured by HR-TEM (see Figures S1 and S2 for particle size distributions); metal dispersions is indicated in parentheses.[d] Measured by a Biolin optical tensiometer.

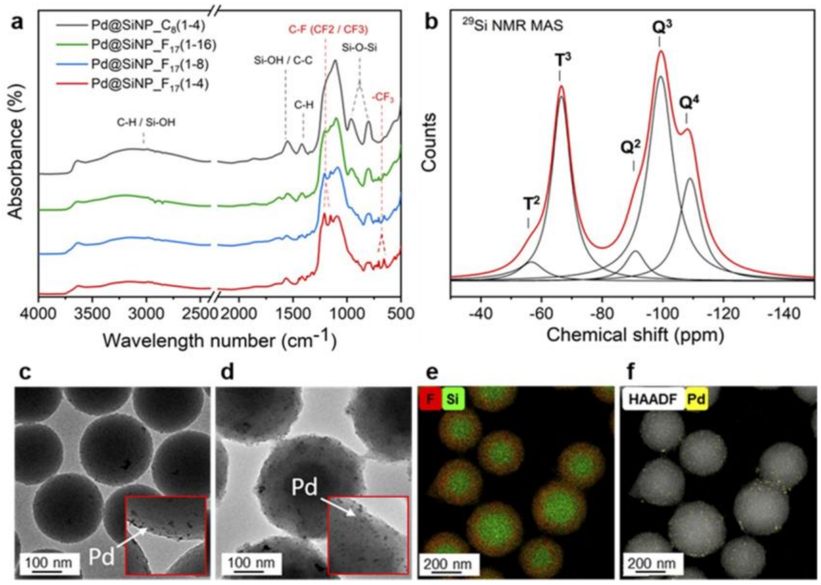

Figure 1. (a) FT-IR spectra of the different particles. (b)^{29}Si NMR MAS spectra of Pd@SiNP_F_{17}(1−4). (c) HR-TEM micrograph of Pd@SiNP_C_8(1−4). (d−f) HR-TEM/EDS micrographs of Pd@SiNP_F_{17}(1−4).

consequence, the gas phase needs to be continuously renewed in catalytic foams to avoid a stoichiometric deficit of gas during the reaction.

Herein, we report the interfacial catalytic properties of an oil foam based on the benzyl alcohol (BnOH)−xylene/air (O_2) system stabilized by surface-active oleophobic (fluorinated) silica particles incorporating Pd nanoparticles. We first addressed the aerobic oxidation of BnOH to evaluate the impact of the experimental conditions such as the stirring rate, particle concentration, surface chemistry of particles, and BnOH/xylene ratio on the foaming and catalytic performance. We then performed the same reaction under O_2 flow, resulting in an enhanced catalytic activity compared to that of a conventional G−L−S stirred-tank reactor with dissolved O_2. The catalytic system is transversal and can be applied to the oxidation of a library of alcohols and cosolvents. The catalytic particles were conveniently recycled after reaction and reused without loss of catalytic performance and surface activity (foamability).

2. RESULTS AND DISCUSSION

2.1. Preparation of Surface-Active Particles.

Fluorinated organosilica particles were synthesized by the Stober method using 1H,1H,2H,2H-perfluorodecyltriethoxysilane (PFDTES), 3-mercaptopropyltriethoxysilane (MPTES), and tetraethyl orthosilicate (TEOS) precursors, with MPTES/PFDTES and TEOS/PFDTES molar ratios of 16 and 4−16, respectively (see the Supporting Information for details). Three fluorinated samples were prepared, which are hereinafter termed SiNP_F_{17}(1−4) (33 wt % F), SiNP_F_{17}(1−8) (25 wt % F), and SiNP_F_{17}(1−16) (15 wt % F) (Table 1, entries 1−3). Besides, a non-fluorinated sample with octyl groups [i.e., SiNP_C_8(1−4)] was prepared by using triethoxy(octyl)silane (C8) as precursor, with MPTES/C_8 and TEOS/C_8 molar ratios of 1 and 4, respectively (Table 1, entry 4). The samples were loaded with Pd nanoparticles by wet impregnation using an ethanol solution of $Pd(OAc)_2$. The final Pd-loaded particles were denoted as Pd@SiNP_F_{17}(1−4) (1.33 wt % Pd), Pd@SiNP_ F_{17}(1−8) (1.49 wt % Pd), Pd@SiNP_F_{17}(1−16) (1.78 wt % Pd), and Pd@SiNP_C_8(1−4) (0.82 wt % Pd). The mean particle size (HR-TEM) was found in the range 300−366 nm for the fluorinated silica particles, whereas it was slightly smaller for Pd@SiNP_C_8(1−4) particles (246 nm) (Table 1 and Figure S1A−D). TG analysis was used to explore the thermal stability of the particles before and after Pd impregnation (Figures S3 and S4). All the samples exhibit a small weight loss until 150 °C (~5%), which can be attributed to water desorption. The parent fluorinated silica particles exhibit a sharp weight loss (ΔW) in the range 400−500 °C, which spans to a broader temperature range (from 220 to 430 °C) after Pd impregnation (Figure S3). The weight loss increases from 23% for Pd@SiNP_F_{17}(1−16) to 38% and 53% for Pd@SiNP_F_{17}(1−8) and Pd@SiNP_F_{17}(1−4), respectively (Table 1). The ΔW/F ratios (w/w) are about 1.5−1.6 for the different samples, matching the expected ratio in PFDTES (1.6). For comparison, SiNP_C_8(1−4) also shows two weight loss regions in the ranges 25−150 °C (~7.5%) and 400−500 °C (~5%), and both decrease after Pd loading (Figure S4). This observation can be explained by the presence of ethoxy groups in SiNP_C_8, which partially hydrolyze during Pd impregnation.

The surface composition of the particles was first analyzed by FT-IR spectroscopy (Figure 1a). Typical bands of silica appear at 1100 and 800 cm^{-1} and can be assigned to asymmetric stretching and bending vibrations of Si−O−Si bonds, respectively.[16] Two additional bands at 3650 and 1610 cm^{-1} are indicative of symmetric stretching and bending vibrations of free Si−OH groups, respectively.[16] A broad band appears in the range 3000−3500 cm^{-1} belonging to Si−OH groups interacting with adsorbed water, reflecting a partial hydrophilic behavior of the particles in line with the mass loss observed in the TG profiles until 150 °C. Characteristic bands ascribed to the fluorocarbon chain appear at 1171 and 1237 cm^{-1} which can be assigned to stretching modes of C−F (CF_2/CF_3) bonds.[16] Additional bands visible at 710 and 670 cm^{-1} are attributed to symmetric stretching bands of CF_3 groups.[17] These bands become more prominent with the fluorine content. Furthermore, bands ascribed to the carbon skeleton appear at 1610 cm^{-1} corresponding to asymmetric stretching modes of C−C groups, and at 2934 and 1462 cm^{-1} which can be assigned to C−H stretching and bending vibrations.[17] No band corresponding to the stretching vibration of S−H groups (2560 cm^{-1}) is observed,[18] which can be explained by the low loading of mercaptopropyl groups on the samples.

The fluorinated particles were further characterized by ^{29}Si, ^{19}F, and ^{13}C NMR MAS before and after Pd impregnation (Figure 1b, Figures S5 and S6). The ^{29}Si NMR MAS spectra exhibit an intense Q_3 resonance band at −99.3 ppm ascribed to Si−OH groups (Figure 1b). A small Q_2 band is also visible at −91.0 ppm revealing the presence of geminal HO−Si−OH groups. The T-region of the spectra is characterized by a sharp T_3 band at −66.6 ppm and a smaller band at −56.8 ppm that are indicative of tripopodal and dipodal moieties on silica, respectively. The ^{19}F NMR MAS spectra display neat signals belonging to the fluorinated chains (Figures S5a and S6a).[19] A sharp signal is observed at −80.7 ppm that can be ascribed to CF_3 groups. Two additional sharp bands are visible at −120.6 and −121.5 ppm which can be ascribed to internal CF_2 groups, as well as a band at −125.3 ppm belonging to the CF_2 group in contact to CF_3. A small band is also observed at −115 ppm which can be tentatively attributed to CF_2 groups in contact to CH_2. The ^{13}C NMR MAS spectra of the particles show combined features of fluorinated and mercaptopropyl chains (Figures S5b and S6b). Two broad and complex bands appear at 109.1 and 115.2 ppm belonging to CF_2 and CF_3 groups in the fluorinated chains.[19b] An additional band is visible at −0.17 ppm which can be assigned to CH_2 groups in fluorinated chains. A sharp and complex band appears at 22.0 ppm which can include the contribution of internal CH_2 groups in mercaptopropyl chains. The characteristic bands appearing at 15.5 and 57.2 ppm are indicative of the presence of CH_3 and CH_2 groups, respectively, in ethoxy groups,[20] and decrease drastically upon Pd impregnation. Finally, a small band is visible at 27.1 ppm which can be ascribed to the C−S groups in mercaptopropyl chains.[21]

Particles were also inspected by HR-TEM (Figure 1c−f and Figure S7). The fluorinated particles consist of a silica core and a fluorinated shell with a thickness increasing with the F loading. Pd nanoparticles, with a mean size in the range 3.6−6.8 nm for the fluorinated particles and 2.9 nm for Pd@SiNP_C_8(1−4) (Table 1 and Figure S2), are well dispersed on the external surface of the particles. XPS analysis reveals similar Pd 3d core level features for all samples (Figure S8a). The $3d_{5/2}$ and $3d_{3/2}$ spin−orbit bands after reduction can be deconvoluted each into two bands centered at 335.1−335.5/336.7−337.7 eV (Pd $3d_{5/2}$) and 340.3−340.9/342.0−343.1 eV (Pd $3d_{3/2}$) for Pd@SiNP_C_8(1−4), Pd@SiNP_F_{17}(1−8), and Pd@SiNP_F_{17}(1−16). These bands are indicative of the presence of Pd^0 and $Pd^{II}O$ species on the particles.[22] The Pd 3d XPS spectrum of Pd@SiNP_F_{17}(1−4) is slightly shifted to higher binding energies with bands centered at 336.3/338.1 eV (Pd $3d_{5/2}$) and 341.5/343.5 eV (Pd $3d_{3/2}$). This suggests a surface enrichment with $Pd^{II}O$ and $Pd^{IV}O_2$ species.[23] The C 1s XPS core level region shows several bands in the range 286.5−293.5 eV for fluorinated particles, which is consistent with the presence of CF_3, CF_2, and CF_2−CH_2 groups (Figure S8b).[24] Additional bands in the range 283.0−286.5 eV are indicative of C−C and CH_2 bonds,[23c] and bands at 293.7 and 296.5 eV are reminiscent of K^+ cations from KBH_4. As expected, all these bands are also visible for Pd@SiNP_C_8(1−4).

The surface activity of the particles is governed by their interaction with the gas and liquid phases, which can be characterized by the interfacial contact angle. Matching the surface chemistry of the particles to a solvent may be challenging, as the range of contact angles where particles are efficient for stabilizing foams is narrow.[25] As an alternative, a mixture of two solvents with different wetting properties may be used to tune the contact angle. Here we chose benzyl alcohol (BnOH) as a model substrate and xylene as cosolvent. Their surface tensions are 39 and 28.9−30.1 mN/m at 20 °C, respectively.[26] The air−BnOH and air−xylene contact angles for the different particles are listed in Table 1. In the case of fluorinated particles, the air−BnOH contact angle decreases from 95.9° for Pd@SiNP_F_{17}(1−4) to 53.2° for Pd@SiNP_F_{17}(1−16), whereas the contact angle is much lower for Pd@SiNP_C_8(1−4) (27.3°). An analogous trend is observed for the air−xylene contact angles, but with lower values. As a matter of fact, the air−xylene contact angle decreases from 53.9° for or Pd@SiNP_F_{17}(1−4) to 11.7° for Pd@SiNP_F_{17}(1−16), while the contact angle for Pd@SiNP_C_8(1−4) is lower than 10°. These observations point out that the Pd@SiNP_C_8(1−4) particle is completely wetted by xylene, while fluorinated particles are wetted partially by both xylene and air, making them good candidates for stabilizing oil foams, especially Pd@SiNP_ F_{17}(1−4).

2.2. Aerobic Oxidation of BnOH. The effect of foaming on the catalytic properties of the different particles was first investigated at variable stirring rates and particle concentrations by using the aerobic oxidation of BnOH as model reaction. These results were further generalized to a range of solvents and alcohols.

The effect of stirring rate was studied over Pd@SiNP_F_{17}(1−4) and Pd@SiNP_C_8(1−4) particles (1 wt %) dispersed in a BnOH/xylene (1:1 v/v) mixture (Figure 2a). Irrespective of the stirring rate, Pd@SiNP_C_8(1−4) does not stabilize foams. In contrast, Pd@SiNP_F_{17}(1−4) can foam, but only at high stirring rates (1000−1500 rpm). In the absence of foam, both particles exhibit similar catalytic performance (Figure 2b). However, in the range 750−1000 rpm, the system with Pd@SiNP_F_{17}(1−4) exhibits a sharp increase of the benzaldehyde (BnAH) yield after 1 h, whereas the yield

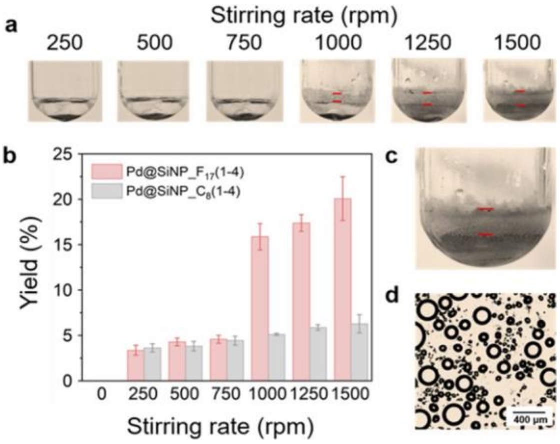

Figure 2. (a) Optical images of the BnOH/xylene (1:1 v/v) system stabilized by 1 wt % Pd@SiNP_F_{17}(1−4) as a function of stirring rate at 80 °C and 1 h. (b) Aerobic oxidation of BnOH over Pd@SiNP_C_8(1−4) and Pd@SiNP_F_{17}(1−4). Reaction conditions: 0.9 mL of BnOH, 0.9 mL of xylene, 1 bar of air, 1 wt % particles, 1500 rpm, 80 °C, 1 h. (c) Zoom-in optical image of BnOH/xylene (1:1 v/v) system stabilized by 1 wt % Pd@SiNP_F_{17}(1−4) at 1500 rpm, 80 °C, 1 h. (d) Microscopic image of BnOH/xylene (1:1 v/v) system stabilized by 1 wt % Pd@SiNP_F_{17}(1−4) at 1500 rpm, 80 °C, 1 h.

remains almost unchanged for Pd@SiNP_C_8(1−4). This large gap in catalytic activity between both particles is attributed to foam generation in the former case (Figure 2c,d). The BnAH yield increases monotonously at higher stirring rates (1000−1500 rpm) for Pd@SiNP_F_{17}(1−4), which can be credited to an increase of foam volume (Figure 2a). We also conducted additional catalytic tests for Pd@SiNP_F_{17}(1−4) as a function of the stirring rate at higher particle loadings. Interestingly, the above trend obtained at 1 wt % loading is also observed when increasing the particle concentration to 2 wt % (Figures S9 and S10). However, at 4 and 6 wt %, the BnAH yield has no break point and displays a monotonous increase at higher stirring rates with systematically higher values compared to Pd@SiNP_C_8(1−4) (Figures S11 and S12).

The catalytic performance was also studied at variable particle concentrations at a fixed stirring rate of 1500 rpm (Figure 3a). For Pd@SiNP_C_8(1−4), the BnAH yield lies below the detection limit for 0.1 and 0.25 wt % particle concentration, whereas it rises monotonously from 2.9% to 16% in the particle concentration range from 0.5 to 10 wt %. In contrast, the BnAH yield exhibits a radically divergent pattern for Pd@SiNP_F_{17}(1−4). In the range 0.1−1 wt %, the yield increases from 5.1% to 25%, which is 5 times higher than that of Pd@SiNP_C_8(1−4). However, the yield remains unchanged at 2 wt %, decreases drastically at 4 wt %, and finally shows a sustained increase beyond this value in a similar fashion to that observed for Pd@SiNP_C_8(1−4).

To gain insight into the above-described abnormal pattern of the BnAH yield for Pd@SiNP_F_{17}(1−4), the effect of particle concentration on the foaming properties was explored. Through vigorous stirring at 1500 rpm, BnOH/xylene foams were prepared at room temperature (Figure S13) and 80 °C (Figure S14). In both cases, the foam volume increases with the particle concentration. However, the foams generated at room temperature are denser and with larger volumes (Figure S15). At 8 wt % particle concentration, almost the entire reactor volume is filled with foam and no free liquid is observed. Besides, these foams are extremely stable (Figure S16): there is no obvious foam degeneration after 24 h, and only slight changes can be devised after 72 h. In contrast, foam stability is much lower at 80 °C (Figure 3c and Figure S17) but improves drastically with the particle concentration. As a matter of fact, at 0.5 wt %, the foam vanishes completely already after 5 min. As the particle concentration increases to 1 wt %, the foam lifetime spreads to 10 min and to 20 and 60

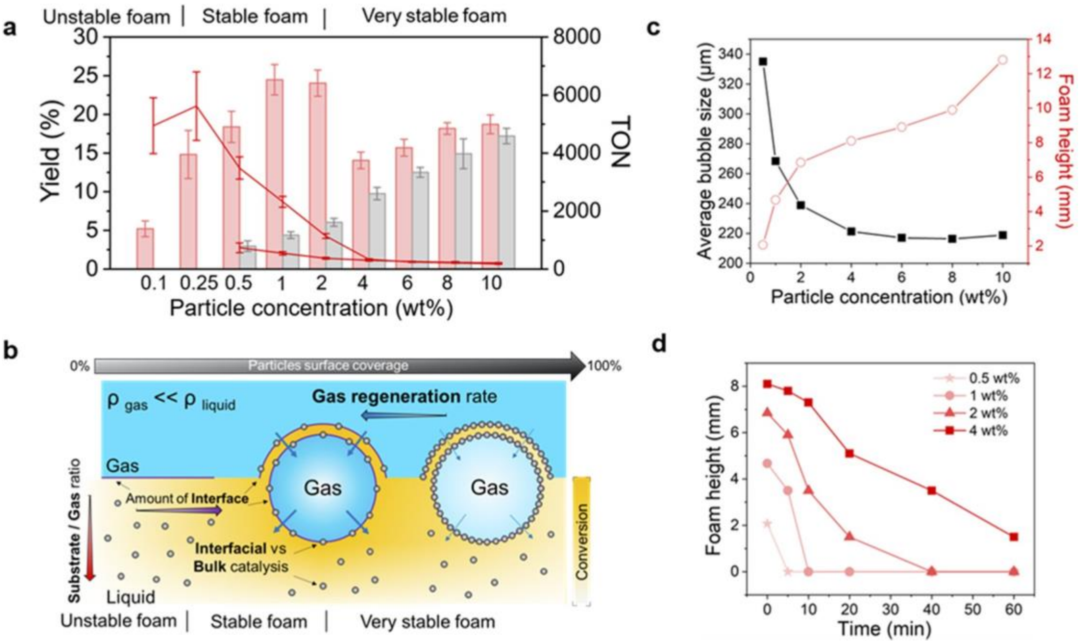

Figure 3. (a) BnAH yield and TON as a function of the particle concentration for the aerobic oxidation of BnOH over Pd@SiNP_C_8(1−4) and Pd@SiNP_F_{17}(1−4). Reaction conditions: 0.9 mL of BnOH, 0.9 mL of xylene, 1 bar air, 1500 rpm, 80 °C, 1 h. (b) Schematic representation of catalysis in particle-stabilized nonaqueous foam system in air. (c) Average bubble size and foam height at variable Pd@SiNP_F_{17}(1−4) particle concentration at 80 °C. (d) Time evolution of the foam height for foam produced with Pd@SiNP_F_{17}(1−4) at 80 °C.

min for foams prepared at 2 and 4 wt %, respectively. This suggests that a higher particle concentration leads to denser shells, reducing bubble coalescence and enhancing foam stability. More information about foam structure was obtained by observing the foams under an optical microscope (Figures S18−S21). At higher particle concentration, the number of bubbles increases at the expense of the bubble size (Figure 3c and Figure S15). This is apparent in the particle concentration range from 0.5 to 4 wt %, where the average bubble size declines from 330 to 250 μm. When the concentration exceeds 4 wt %, the average bubble size hardly changes, remaining around 230 μm. It is worth mentioning that nonspherical bubbles are visible for foams generated at 80 °C, providing evidence of a jammed G−L interface; that is, bubbles are covered by a close-packed layer (or multilayer) of particles.

From the foam analysis above, the following conclusions can be drawn to rationalize the catalytic performance of Pd@SiNP_F$_{17}$(1−4). At very low particle concentrations, the foam is rather unstable and the foam volume is small (and so the interface available for the reaction), leading to low BnAH yield ("unstable foam" regime, Figure 3b). An increase of the particle concentration up to 2 wt % results in a remarkable increase of the foam volume with concomitant increase of the BnAH yield ("stable foam" regime, Figure 3b). The foam height remains nearly constant at 4 wt % particle concentration, but the interfacial area increases because of the formation of smaller bubbles. Most importantly, at this particle concentration, a majority of the bubbles are covered by a close-packed layer of particles, resulting in a very stable foam with a collapse time longer than the reaction time (Figure 3d). This has a very important consequence: the O_2 concentration becomes the limiting factor, as O_2 in the bubbles cannot be regenerated by their collapse and restitution ("very stable foam" regime, Figure 3b). As a result, a similar catalytic performance is observed for nonfoaming and foaming systems above 4 wt %. This body of results points out that intermediate particle concentrations are required for enhancing the catalytic activity in the presence of foam, boosting the interfacial area while maintaining the permeability of the particle layer and allowing fast gas regeneration.

We first compared the catalytic performance of Pd@SiNP_F$_{17}$(1−4) particles alone at 0.5 wt % concentration and in a mixture with noncatalytic SiNP_F$_{17}$(1−4) particles at 0.5 wt % concentration each (Figure 4a−d). Both systems perform similarly (Figure 4a vs Figure 4b). However, a slight increase of the foam volume is observed for the mixed system, suggesting preferential adsorption of noncatalytic (but better foaming) particles at the G−L interface. In contrast, when 1 wt % noncatalytic SiNP_F$_{17}$(1−4) and 1 wt % Pd@SiNP_F$_{17}$(1−4) particles are mixed together, the BnAH yield is much lower than that measured with 1 wt % Pd@SiNP_F$_{17}$(1−4) particles only (Figure 4c vs Figure 4d), even if the foam volume is much larger in the mixed system. These results suggest that the interface is predominantly populated by noncatalytic particles, which is in line with the increase in the foam volume. In contrast, catalytic particles are mainly dispersed in the bulk solvent, resulting in a lower catalytic activity.

In the examples above, both particles were surface-active and accordingly the actual composition of the G−L interface remains unknown. To gain better insight into the effect of the interface composition, we performed additional catalytic and foaming tests using a mixture of surface-active but noncatalytic SiNP_F$_{17}$(1−4) particles and catalytic but non-surface-active Pd@SiNP_C$_8$(1−4) particles, favoring the location of the former at the interface and the latter in the bulk solvent. First, 0.5 wt % SiNP_F$_{17}$(1−4) particles were mixed with 0.5 wt % Pd@SiNP_C$_8$(1−4) particles (Figure 4f). This system generates a foam similar to that observed with 0.5 wt % catalytic/foaming Pd@SiNP_F$_{17}$(1−4) particles (Figure 4a). At the same time, despite the formation of foam, the system shows very low yield (<5%). Also, low yield (<5%) is observed by using 0.5 wt % Pd@SiNP_C$_8$(1−4) particles only without foam (Figure 4e). These results confirm that as expected, only SiNP_F$_{17}$(1−4) particles adsorb at the G−L interface, while the catalytic Pd@SiNP_C$_8$(1−4) particles are dispersed in the bulk solvent where they demonstrate poor catalytic performance. This phenomenon becomes more prominent when the Pd@SiNP_C$_8$(1−4) particle concentration is further increased to 1 wt % (Figure 4g). The yield in this case is only 5%, which is 5 times lower than that obtained with 1 wt % of surface-active catalytic Pd@SiNP_F$_{17}$(1−4) particles (Figure 4c). Interestingly, the yield obtained in the presence of foam is slightly lower than in nonfoaming system (Figure 4h vs Figure 4g), indicating a negative role of the foam in this case, arising most likely from a lower gas exchange rate.

2.3. Effect of Liquid Phase Composition on Catalytic Performance. As pointed out above, the foaming and catalytic performance of the studied systems are closely related. We therefore investigated the effect of the BnOH/xylene volume ratio on the foamability and measured the contact angles at room temperature as descriptors of the particle wetting by two phases. Note that the interfacial contact angle is sensitive to the temperature (the reactions were

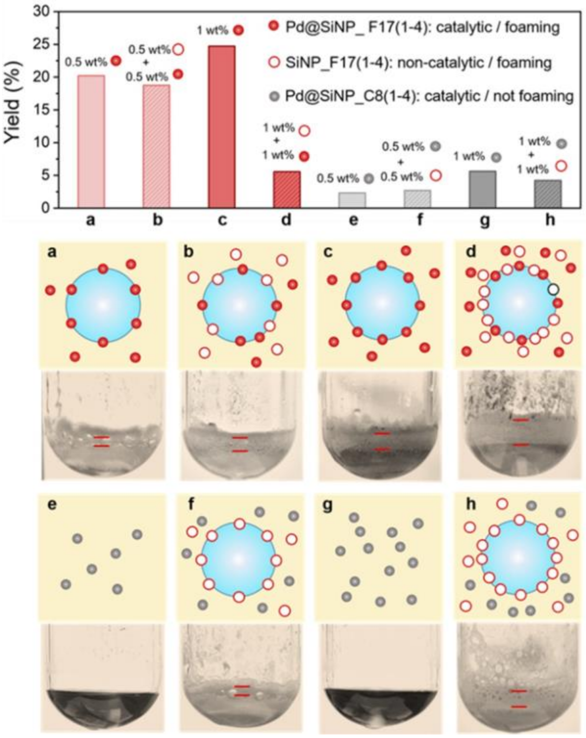

Figure 4. Top: aerobic oxidation of BnOH catalyzed by a mixture of catalytic and noncatalytic particles. Bottom: schematic representation and optical images of reaction system after 1 h reaction. Reaction conditions: 0.9 mL of BnOH, 0.9 mL of xylene, 1 bar of air, 1500 rpm, 80 °C, 1 h.

conducted at 80 °C), and accordingly the room-temperature contact angles should be regarded as indicative.

Two particles with high fluorine content, i.e., Pd@SiNP_F$_{17}$(1−4) and Pd@SiNP_F$_{17}$(1−8), can stabilize foams for most of the mixtures (Figure 5a, left; Figures S22 and S23). Pd@SiNP_F$_{17}$(1−4) particles generate stable foams for BnOH/xylene volume ratios ranging from 1:5 to 4:2 (contact angle from 60° to 73°), with the foam height increasing with the BnOH content. At 5:1 BnOH/xylene ratio, the contact angle is 79° and particles are badly wetted by the liquid, resulting in almost no foam formation. In pure BnOH, these particles cannot be dispersed at all (contact angle 96°). As a consequence, no foam is produced. Pd@SiNP_F$_{17}$(1−8) particles at a 1:5 BnOH/xylene ratio are overwetted by the liquid and cannot foam (contact angle lower than 40°)□only individual bubbles are visible. Foamability increases with the BnOH content, reaching a maximum in the range of BnOH/xylene ratios from 3:3 to 5:1 (contact angles 48° and 58°, respectively). Pd@SiNP_F$_{17}$(1−16) particles with the lowest fluorine content exhibit poor foamability for all compositions (Figure 5a) due to overwetting by the solvent (contact angles lower than 50°), and Pd@SiNP_C$_8$(1−4) particles generate no foam at all. Overall, good foaming is achieved for systems with a room-temperature contact angle in the range 50°−80° (Figure 5a, right; Figures S24−S26).

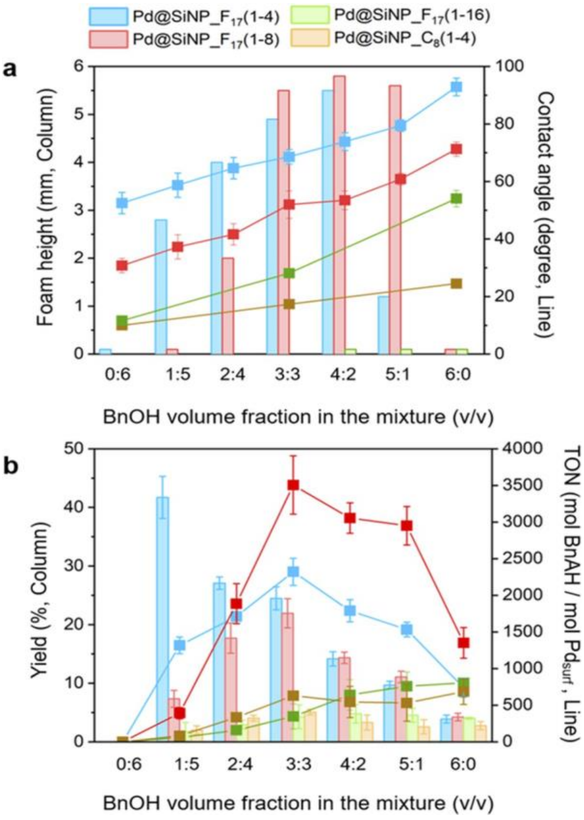

Figure 5. (a) Interfacial contact angle and foam height as a function of the BnOH concentration over Pd@SiNP_C$_8$(1−4), Pd@SiNP_F$_{17}$(1−4), Pd@SiNP_F$_{17}$(1−8), and Pd@SiNP_F$_{17}$(1−16) particles. (b) BnAH yield and TON after 1 h in the aerobic oxidation of BnOH over Pd@SiNP_C$_8$(1−4), Pd@SiNP_F$_{17}$(1−4), Pd@SiNP_F$_{17}$(1−8), and Pd@SiNP_F$_{17}$(1−16) particles in BnOH/xylene mixtures at variable BnOH/xylene volume ratios. Reaction conditions: 1.8 mL total liquid volume, 1 wt % particles, 1 bar air, 1500 rpm, 80 °C, 1 h.

The catalytic performance of the different particles was also studied at variable BnOH/xylene volume ratios (Figure 5b). Non-surface-active Pd@SiNP_C$_8$(1−4) and overwetted Pd@SiNP_F$_{17}$(1−16) particles show very low BnAH yield (<5%). In contrast, more oleophobic Pd@SiNP_F$_{17}$(1−4) and Pd@SiNP_F$_{17}$(1−8) particles generate a significant amount of foam which results in much higher yield for these systems. In both cases, the TON evolves alongside foaming with a maximum value for 3:3 BnOH/xylene mixtures at 2300 and 3500 mol BnAH/mol Pd$_{surf}$ for Pd@SiNP_F$_{17}$(1−4) and Pd@SiNP_F$_{17}$(1−8) particles, respectively. The TON decreases at higher BnOH volume fractions, which is not in line with the foam evolution. Accordingly, other factors should be at play. Detailed analysis at this stage appears challenging, as the BnOH/xylene volume ratio changes not only the substrate concentration but also the surface tension of the liquid phase and the interfacial contact angle, affecting the foam volume and interfacial concentration of particles.

Given the high activity of Pd@SiNP_F$_{17}$(1−4) and Pd@SiNP_F$_{17}$(1−8) particles, the kinetic profiles were measured for both catalytic particles at 80 °C and variable BnOH/xylene volume ratios (Figure 6). In the case of Pd@SiNP_F$_{17}$(1−4) (Figure 6a), the BnAH yield increases faster at lower BnOH/xylene ratios, reaching almost 100% for 1:5 BnOH/xylene mixtures after 4 h. At higher BnOH/xylene ratios (i.e., 3:3, 4:2,

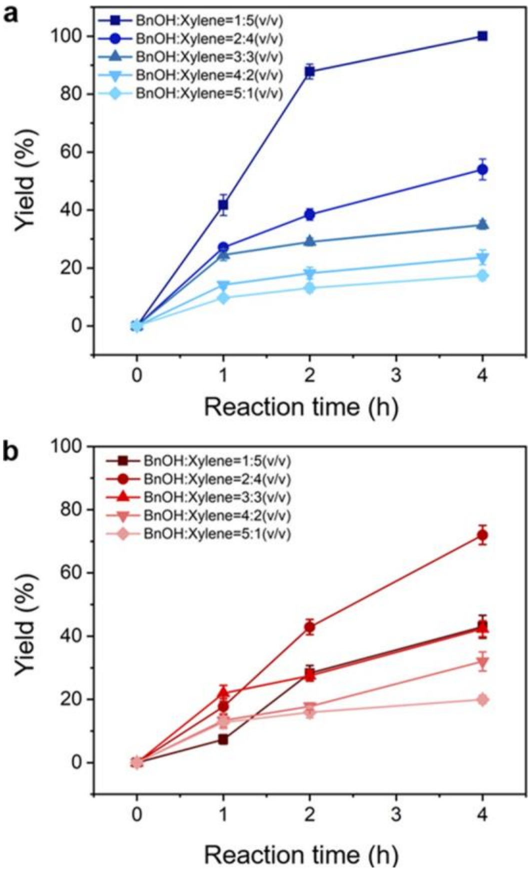

Figure 6. (a) Kinetic profiles for the aerobic oxidation of BnOH over (a) Pd@SiNP_F$_{17}$(1−4) and (b) Pd@SiNP_F$_{17}$(1−8). Reaction conditions: 0.9 mL of BnOH, 0.9 mL of xylene, 1 wt % particle, 1 bar air, 1500 rpm, 80 °C.

and 5:1), the reaction is slowed after 1 h, most likely due to foam stabilization and coarsening as more particles are brought to the surface, reducing O_2 regeneration. The catalytic activity a t = 0 (turnover frequency, TOF_0) increases with the BnOH/xylene ratio from 1400 h^{-1} (1:5) to a maximum value of 3400 h^{-1} (3:3), followed by a decrease until 2100 h^{-1} (5:1). This trend is consistent with that observed for the TON in Figure 5b. In the case of Pd@SiNP_F$_{17}$(1−8) particles, the reaction is not slowed after 1 h (Figure 6b), which can be explained by a lower foam stability compared to Pd@SiNP_F$_{17}$(1−4) at equal reaction conditions, allowing higher permeability and faster O_2 regeneration in the bubbles. A maximum value of TOF_0 is also observed for 3:3 BnOH/xylene mixtures (5400 h^{-1}), while a highest yield is achieved for 2:4 BnOH/xylene mixtures (72% after 4 h).

2.4. Catalyst Recyclability and Reuse. The recyclability and reuse of Pd@SiNP_F$_{17}$(1−4) particles were studied for the aerobic oxidation of BnOH over seven consecutive cycles. After each cycle, the reaction media was centrifuged (4500 rpm, 3 min), and the particles were separated, washed with acetone for three times, and dried at 80 °C for 4 h before use in the subsequent cycle. The particles can be conveniently recycled for at least seven times without appreciable loss of catalytic activity and foamability (Figure 7). No Pd leaching is observed during the reaction, as inferred by ICP-OES.

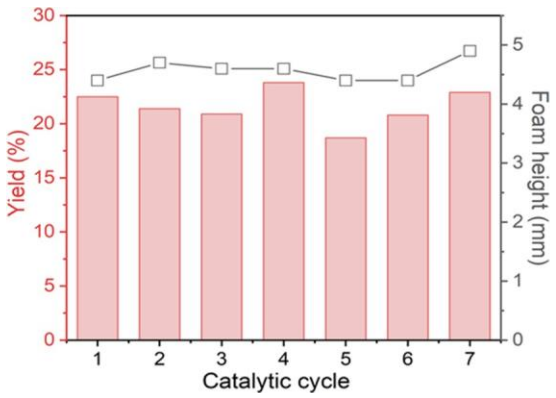

Figure 7. Recyclability and reuse of Pd@SiNP_F$_{17}$(1−4) for the aerobic oxidation of BnOH over seven consecutive cycles. Reaction conditions: 0.9 mL of BnOH, 0.9 mL of xylene, 1 wt % particle, 1 bar air, 1500 rpm, 80 °C, 1 h.

2.5. Solvent Scope. Pd@SiNP_F$_{17}$(1−4) particles cannot be dispersed in pure BnOH (contact angle 96°, surface tension 39 mN/m at 20 °C) and therefore require a cosolvent. In order to explore if xylene in the reaction mixture may be replaced by other liquids, we performed the aerobic oxidation of BnOH with a series of solvents at a fixed BnOH/solvent volume ratio of 1:5 (Figure S27−S29). All solvents have three common characteristics: their boiling point exceeds 160 °C, they are miscible with BnOH at 80 °C, and are inert at this temperature. Cosolvents with lower surface tension such as DIBK (23.92 mN/m at 20 °C), dodecane (25.4 mN/m at 20 °C), hexylene glycol (33.1 mN/m at 20 °C) can be used to prepare foams. The catalytic performance in these systems is similar or higher than that in BnOH/Xylene mixture. In contrast, DMSO, with a higher surface tension than BnOH, cannot be used to stabilize foams, since the mixture cannot wet the particles. This leads to a poor catalytic performance for this system.

2.6. Catalytic Tests in O_2 Flow. The BnOH oxidation reaction was further studied in O_2 flow at ambient pressure in a 3:3 BnOH/xylene mixture with 1 wt % Pd@SiNP_F$_{17}$(1−4) at 1500 rpm stirring rate. The BnAH yield after 1 h is 48% (Table S1), which almost doubles that obtained under air (25%) and is 7 times higher than the yield over Pd@SiNP_C$_8$(1−4) without foam (6.4%) (Figure 5a). These results are predictable for a nonzero reaction order of O_2, as pure O_2 provides higher reactant concentration compared to air, enhancing the reaction rate. No apparent effect of the O_2 flow rate [range 10−100 mL (STP)/min] on the BnAH yield is observed.

The reaction was also performed in the presence of O_2 flow at higher temperature. The yields are 74% and 96% at 100 and 120 °C, respectively (Table S1). In all cases, foams are generated and show similar appearance (Figure S30). Replacing xylene by dodecane allows conducting the reaction at higher temperature. In the presence of dodecane, a similar yield of 93% is attained at 120 °C, and the reaction can reach 89% at 140 °C after only 30 min.

2.7. Aromatic Alcohol Scope. We also examined the generality of aromatic alcohol oxidation in foam systems under O_2 flow (Table S2, Figures S31 and S32). The results obtained with xylene as a solvent clearly demonstrate higher activity of foam systems in the oxidation of aromatic alcohols as compared to nonfoam systems. For 1-phenylethanol, the acetophenone yield in the foam system (Pd@SiNP_F$_{17}$(1−4) particles) after 1 h reaction is 7.1%, 23%, and 50% at 80, 100, and 120 °C, respectively. This is 7 times higher than the values in nonfoam system (Pd@SiNP_C$_8$(1−4) particles) at the same temperature. The combination of benzyl alcohol and 1-phenylethanol (1:1.2 mol/mol) in xylene (1:2 v/v in xylene for each alcohol) results in a yield of 92% and 28%, respectively, which are comparable to the values measured on the single alcohols. The conversion of methylbenzyl alcohol into the corresponding aldehyde in the presence of foam is 48% at 120 °C after 1 h, while the yield is only 7.1% in nonfoam system. Vanillyl alcohol is completely converted into vanillin at 110 °C after 1 h in foam system, while the conversion only reaches 12% in nonfoam system. The oxidation of cinnamyl alcohol was studied at variable temperatures. The yield of cinnamaldehyde at 100 °C after 2 h in the nonfoam system is 25%, which is lower than the value measured at 80 °C after 1 h in the presence of foam (31%). The yield increases to 92% at full cinnamyl alcohol conversion after reaction at 120 °C for 30 min with only minor amounts of benzaldehyde and ethylbenzene as byproducts. The yield of coniferyl aldehyde from coniferyl alcohol, which is directly derived from lignin, is 60% at 120 °C after 2 h in the presence of foam, while the yield is only 5.1% in nonfoam system. Additional byproducts are observed resulting from pathways involving phenoxy radicals.[27]

2.8. Extension to Aliphatic Alcohols. In addition to aromatic alcohols, we developed foam systems for the aerobic oxidation of aliphatic alcohols stabilized by Pd@SiNP_F$_{17}$(1−4) particles in O_2 flow using diisobutyl ketone (DIBK) as solvent (Table S2, Figure S33). In all cases, higher activity of foam systems is obtained compared to nonfoam systems in the presence of Pd@SiNP_C$_8$(1−4) particles. The oxidation of 1-octanol at 160 °C after 4 h results in the formation of octyl octanoate with 50% yield. In contrast, only product traces are observed without foam. Likewise, the oxidation of 2-octanol at the same reaction conditions results in 58% yield of 2-octanone in the presence of foam, whereas the nonfoam system shows only 0.9% yield of product. Finally, 1-octen-3-ol shows higher reactivity, reaching more than 99% yield of 1-octen-3-one at 120 °C after 1 h in the presence of foam. In contrast, a control experiment without foam only shows 10% yield of product. Overall, these results clearly show the versatility of foam systems for the aerobic oxidation of aliphatic alcohols at ambient pressure.

3. CONCLUSIONS

In summary, we prepared oil foams stabilized by surface-active silica particles bearing fluorinated chains and Pd nanoparticles. Foamability increased with both the particle concentration and stirring rate. High foam stability was achieved in benzyl alcohol/xylene mixtures even at very low particle concentration (<1 wt %) provided that the contact angle locates in the range 41°−73°. However, it declined drastically upon heating from room temperature to 80 °C. The catalytic performance was strongly affected by the foaming properties, with 8 times activity increase in pure O_2 compared to nonfoam systems. Intermediate foam stability was required to achieve good catalytic activity, combining a large interfacial area and high gas exchange rate. Preferential location of the catalytic particles at the G−L interface was found even more important for catalytic performance than foamability. Particles were conveniently recycled with high foamability and catalytic efficiency maintained for at least seven consecutive runs. Besides xylene, other solvents with surface tension lower than that of the substrate could tune the particle wettability, enhancing the foamability and catalytic performance in the aerobic oxidation of a panel of aromatic alcohols. Most interestingly, foam systems could be developed by using diisobutyl ketone as solvent for the aerobic oxidation of aliphatic alcohols. This demonstrates the universality of our approach and allows performing reactions at higher temperatures. Overall, this study paves the way to the reengineering of G−L−S reactors for oxidation reactions at low air/O_2 pressures.

Corresponding Author

Marc Pera-Titus − UMI 3464 CNRS, Solvay, Eco-Efficient Products and Processes Laboratory (E2P2L), 201108 Shanghai, China; Cardiff Catalysis Institute, School of Chemistry, Cardiff University, Cardiff CF10 3AT, U.K.; orcid.org/0000-0001-7335-1424; Email: peratitusm@cardiff.ac.uk

Authors

Shi Zhang − UMI 3464 CNRS, Solvay, Eco-Efficient Products and Processes Laboratory (E2P2L), 201108 Shanghai, China; Laboratoire du Futur, UMR 5258 CNRS, Université de Bordeaux, 33603 Cedex Pessac, France
Dmytro Dedovets − Laboratoire du Futur, UMR 5258 CNRS, Université de Bordeaux, 33603 Cedex Pessac, France; orcid.org/0000-0002-9040-2614
Andong Feng − UMI 3464 CNRS, Solvay, Eco-Efficient Products and Processes Laboratory (E2P2L), 201108 Shanghai, China; Laboratoire du Futur, UMR 5258 CNRS, Université de Bordeaux, 33603 Cedex Pessac, France
Kang Wang − Cardiff Catalysis Institute, School of Chemistry, Cardiff University, Cardiff CF10 3AT, U.K.

Notes

The authors declare no competing financial interest.

This study was funded by the ERC grant Michelangelo (Contract #771586).

REFERERENCES

(1) (a) Shah, Y. T. Gas-Liquid-Solid Reactor Design; McGraw-Hill:

ASSOCIATED CONTENT

Particle size distribution of the different particles; size distribution of Pd nanoparticles; TGA profiles, ^{13}C NMR MAS and XPS spectra, and HR-TEM images of the different particles; effect of the stirring rate and particle loading on the aerobic oxidation reaction of BnOH over different particles at 80 °C; optical images of the BnOH/xylene foams at 80 °C at variable stirring rates and particle loadings after reaction; average bubble size and BnOH/xylene foam height at variable stirring rate particle loading and BnOH/xylene volume ratio as a function of time; photos of contact angles of liquid drops in air on particle pellets; effect of the solvent on BnOH oxidation; optical images of BnOH/solvent/air foams at 80 °C; optical images of BnOH/solvent/O_2 foams at variable temperatures; optical images of coniferyl alcohol/dodecane/air, 1-octen-3-ol/DIBK, 1-octanol/DIBK, and 2-octanol/DIBK foams; catalytic results for BnOH oxidation in O_2 flow; substrate scope expansion for catalytic tests in O_2 flow (PDF)

New York, 1979. (b) Ramachandran, P. A.; Chaudari, R. V. Three-Phase Catalytic Reactors; Topics in Chemical Engineering; Gordon and Breach Science Publishers: Philadelphia, 1983; Vol. 2, Chapter 9. (c) Trambouze, P.; Euzen, J. P. Chemical Reactors: From Design to Operation; Editions Technip: Paris, 2004. (d) Henkel, K.-D. Reactor Types and Their Industrial Applications. In Ullmann's Encyclopedia of Industrial Chemistry; Wiley-VCH: Weinheim, 2012; Vol. 31, pp 293−327.

(2) (a) Kobayashi, J.; Mori, Y.; Okamoto, K.; Akiyama, R.; Ueno, M.; Kitamori, T.; Kobayashi, S. A Microfluidic Device for Conducting Gas-Liquid-Solid Hydrogenation Reactions. Science 2004, 304, 1305−1308. (b) Jähnisch, K.; Hessel, V.; Lowe, H.; Baerns, M. Chemistry in Microstructured Reactors. Angew. Chem., Int. Ed. 2004, 43, 406. (c) Hessel, V.; Angeli, P.; Gavriilidis, A.; Löwe, H. Gas-Liquid and Gas-Liquid-Solid Microstructured Reactors: Contacting Principles and Applications. Ind. Eng. Chem. Res. 2005, 44, 9750−9769. (d) Irfan, M.; Glasnov, T. N.; Kappe, C. O. Heterogeneous Catalytic Hydrogenation Reactions in Continuous-Flow Reactors. ChemSusChem 2011, 4, 300−316. (e) Dencic, I.; Hessel, V.; de Croon, M. H. J. M.; Meuldijk, J.; van der Doelen, C. W. J.; Koch, K. Recent Changes in Patenting Behavior in Microprocess Technology and its Possible Use for Gas-Liquid Reactions and the Oxidation of Glucose. ChemSusChem 2012, 5, 232−245. (f) Brzozowski, M.; O'Brien, M.; Ley, S. V.; Polyzos, A. Flow Chemistry: Intelligent Processing of Gas-Liquid Transformations Using a Tube-in-Tube Reactor. Acc. Chem. Res. 2015, 48, 349−362. (g) Gutmann, B.; Cantillo, D.; Kappe, C. O. Continuous-Flow Technology − a Tool for the Safe Manufacturing of Active Pharmaceutical Ingredients. Angew. Chem., Int. Ed. 2015, 54, 6688−6728. (h) Yeong, K. K.; Gavriilidis, A.; Zapf, R.; Hessel, V. Catalyst Preparation and Deactivation Issues for Nitrobenzene

Hydrogenation in a Microstructured Falling Film Reactor. Catal. Today 2003, 81, 641−651. (i) Yeong, K. K.; Gavriilidis, A.; Zapf, R.; Hessel, V. Experimental Studies of Nitrobenzene Hydrogenation in a Microstructured Falling Film. Reactor. Chem. Eng. Sci. 2004, 59, 3491−3494.

(3) (a) Ræder, H.; Bredesen, R.; Crehan, G.; Miachon, S.; Dalmon, J.-A.; Pintar, A.; Levec, J.; Torp, E. G. Wet Air Oxidation Process Using a Catalytic Membrane Contactor. Sep. Purif. Technol. 2003, 32, 349−355. (b) Reif, M.; Dittmeyer, R. Porous, Catalytically Active Ceramic Membranes for Gas-Liquid Reactions: a Comparison Between Catalytic Diffuser and Forced Through Flow Concept. Catal. Today 2003, 82, 3−14. (c) Miachon, S.; Dalmon, J.-A. Catalysis in Membrane Reactors: What About the Catalyst? Top. Catal. 2004, 29, 59−65.

(4) (a) Pera-Titus, M.; Leclercq, L.; Clacens, J. M.; De Campo, F.; Nardello-Rataj, V. Pickering Interfacial Catalysis for Biphasic Systems: From Emulsion Design to Green Reactions. Angew. Chem., Int. Ed. 2015, 54, 2006−2021. (b) Bago Rodriguez, A. M.; Binks, B. P. Catalysis in Pickering Emulsions. Soft Matter 2020, 16, 10221−10243.

(5) (a) Drenckhan, W. Generation of Superstable, Monodisperse Microbubbles Using a pH-Driven Assembly of Surface-Active Particles. Angew. Chem., Int. Ed. 2009, 48, 5245−5347. (b) Horozov, T. S. Foams and Foam Films Stabilised by Solid Particles. Curr. Opin. Colloid Interface Sci. 2008, 13, 134−140. (c) Paunov, V. N.; Al-Shehri, H.; Horozov, T. S. Attachment of Composite Porous Supra-Particles to Air-Water and Oil-Water Interfaces: Theory and Experiment. Phys. Chem. Chem. Phys. 2016, 18, 26495−26508.

(6) Huang, Z.; Li, F.; Chen, B.; Yuan, G. Sustainable Catalytic Oxidation of Alcohols over the Interface Between Air and Water. Green Chem. 2015, 17, 2325−2329.

(7) Huang, J.; Cheng, F.; Binks, B. P.; Yang, H. PH-Responsive Gas-Water-Solid Interface for Multiphase Catalysis. J. Am. Chem. Soc. 2015, 137, 15015−15025.

(8) Binks, B. P.; Horozov, T. S. Aqueous Foams Stabilized Solely by Silica Nanoparticles. Angew. Chem., Int. Ed. 2005, 44, 3722−3725.

(9) (a) Alargova, R. G.; Warhadpande, D. S.; Paunov, V. N.; Velev, O. D. Foam Superstabilization by Polymer Microrods. Langmuir 2004, 20, 10371−10374. (b) Ito, M.; Takano, K.; Hanochi, H.; Asaumi, Y.; Yusa, S.-I.; Nakamura, Y.; Fujii, S. pH-Responsive Aqueous Bubbles Stabilized with Polymer Particles Carrying Poly(4-vinylpyridine) Colloidal Stabilizer. Front. Chem. 2018, 6, 1−10. (c) Guillermic, R. M.; Saint-Jalmes, A. Dynamics of Poly-nipam Chains in Competition with Surfactants at Liquid Interfaces: From Thermoresponsive Interfacial Rheology to Foams. Soft Matter 2013, 9, 1344−1353. (d) Yang, P.; Mykhaylyk, O. O.; Jones, E. R.; Armes, S. P. RAFT Dispersion Alternating Copolymerization of Styrene with N-Phenylmaleimide: Morphology Control and Application as an Aqueous Foam Stabilizer. Macromolecules 2016, 49, 6731−6742. (e) Dupin, D.; Howse, J. R.; Armes, S. P.; Randall, D. P. Preparation of Stable Foams Using Sterically Stabilized pH-Responsive Latexes Synthesized by Emulsion Polymerization. J. Mater. Chem. 2008, 18, 545−552. (f) Binks, B. P.; Murakami, R.; Armes, S. P.; Fujii, S.; Schmid, A. PH-Responsive Aqueous Foams Stabilized by Ionizable Latex Particles. Langmuir 2007, 23, 8691−8694. (g) Fujii, S.; Mochizuki, M.; Aono, K.; Hamasaki, S.; Murakami, R.; Nakamura, Y. PH-Responsive Aqueous Foams Stabilized by Hairy Latex Particles. Langmuir 2011, 27, 12902−12909. (h) Fujii, S.; Akiyama, K.; Nakayama, S.; Hamasaki, S.; Yusa, S.-I.; Nakamura, Y. PH- and Temperature-Responsive Aqueous Foams Stabilized by Hairy Latex Particles. Soft Matter 2015, 11, 572−579. (i) Nakayama, S.; Hamasaki, S.; Ueno, K.; Mochizuki, M.; Yusa, S.; Nakamura, Y.; Fujii, S. Foams Stabilized with Solid Particles Carrying Stimuli-Responsive Polymer Hairs. Soft Matter 2016, 12, 4794−4804.

(10) (a) Hu, Z.; Xu, R. E.; Cranston, D.; Pelton, R. H. Stable Aqueous Foams from Cellulose Nanocrystals and Methyl Cellulose. Biomacromolecules 2016, 17, 4095−4099. (b) Tenhunen, T.-M.; Pöhler, T.; Kokko, A.; Orelma, H.; Schenker, M.; Gane, P.; Tammelin, T. Enhancing the Stability of Aqueous Dispersions and Foams Comprising Cellulose Nanofibrils (CNF) with $CaCO_3$ Particles. Nanomaterials 2018, 8, 651−668. (c) Weißenborn, E.; Braunschweig, B. Hydroxypropyl Cellulose as a Green Polymer for Thermo-Responsive Aqueous Foams. Soft Matter 2019, 15, 2876−2883.

(11) Binks, B. P.; Shi, H. Aqueous Foams in the Presence of Surfactant Crystals. Langmuir 2020, 36, 991−1002.

(12) (a) Murakami, R.; Bismarck, A. Particle-Stabilized Materials: Dry Oils and (Polymerized) Non-Aqueous Foams. Adv. Funct. Mater. 2010, 20, 732−737. (b) Binks, B. P.; Rocher, A.; Kirkland, M. Oil Foams Stabilised Solely by Particles. Soft Matter 2011, 7, 1800−1808. (c) Binks, B. P.; Rocher, A. Stabilisation of Liquid-Air Surfaces by Particles of Low Surface Energy. Phys. Chem. Chem. Phys. 2010, 12, 9169−9171.

(13) (a) Binks, B. P.; Tyowua, A. T. Influence of the Degree of Fluorination on the Behaviour of Silica Particles at Air-Oil Surfaces. Soft Matter 2013, 9, 834−845. (b) Binks, B. P.; Sekine, T.; Tyowua, A. T. Dry Oil Powders and Oil Foams Stabilised by Fluorinated Clay Platelet Particles. Soft Matter 2014, 10, 578−589. (c) Lai, Y.; Zhou, H.; Zhang, Z.; Tang, Y.; Ho, J. W. C.; Huang, J.; Tay, Q.; Zhang, K.; Chen, Z.; Binks, B. Multifunctional TiO_2-Based Particles: The Effect of Fluorination Degree and Liquid Surface Tension on Wetting Behavior. P. Part. Part. Syst. Charact. 2015, 32, 355−363. (d) Binks, B. P.; Johnston, S. K.; Sekine, T.; Tyowua, A. T. Particles at Oil-Air Surfaces: Powdered Oil, Liquid Oil Marbles, and Oil Foam. ACS Appl. Mater. Interfaces 2015, 7, 14328−14337.

(14) Dyab, A. K. F.; Al-Haque, H. N. Particle-Stabilised Non-Aqueous Systems. RSC Adv. 2013, 3, 13101−13105.

(15) Fameau, A. L.; Saint-Jalmes, A. Non-Aqueous Foams: Current Understanding on the Formation and Stability Mechanisms. Adv. Colloid Interface Sci. 2017, 247, 454−464.

(16) Chukin, G. D.; Malevich, V. I. Infrared Spectra of Silica. J. Appl. Spectrosc. 1977, 26, 223−229.

(17) Shahabadi, S. M. S.; Rabiee, H.; Seyed, S. M.; Mokhtare, A.; Brant, A. Superhydrophobic Dual Layer Functionalized Titanium Dioxide/Polyvynylidene Fluoride-co-Hexafluoropropylene (TiO_2/PH) Nanofibrous Membrane for High Flux Membrane Distillation. J. Membr. Sci. 2017, 537, 140−150.

(18) Senkevich, J. J.; Mitchell, C. J.; Yang, G.-R.; Lu, T.-M. Surface Chemistry of Mercaptan and Growth of Pyridine Short-Chain Alkoxy Silane Molecular Layers. Langmuir 2002, 18, 1587−1594.

(19) (a) van Ravenstein, L.; Ming, W.; van de Grampel, R. D.; van der Linde, R.; de With, G.; Loontjens, T.; Thune, P. C.; Niemantsverdriet, J. W. Low Surface Energy Polymeric Films From Novel Fluorinated Blocked Isocyanates. Macromolecules 2004, 37, 408−413. (b) Chen, Q.; Schmidt-Rohr, K. 19F and 13C NMR Signal Assignment and Analysis in a Perfluorinated Ionomer (Nafion) by Two-Dimensional Solid-State NMR. Macromolecules 2004, 37, 5995−6003.

(20) Li, Y.; Zhao, G.; Hong, B.; Zhao, S.-L.; Han, X.; Pera-Titus, M. Unraveling Particle Size and Roughness Effects on the Interfacial Catalytic Properties of Pickering Emulsions. Colloids Surf., A 2020, 599, 124800.

(21) Ashu-Arrah, B. A.; Glennon, J. D.; Albert, K. Synthesis and Characterization of Bonded Mercaptopropyl Silica Intermediate Stationary Phases Prepared Using Multifunctional Carbon Dioxide as a Reaction Solvent. J. Chromatogr., A 2012, 1222, 38−45.

(22) (a) Engler, B. H.; Lindner, D.; Lox, E. S.; Schafer-Sindlinger, A.; Ostgathe, K. Development of Improved Pd-Only and Pd/Rh Three-Way Catalysts. Stud. Surf. Sci. Catal. 1995, 96, 441−460. (b) Otto, K.; Haack, L. P.; deVries, J. E. Identification of Two Types of Oxidized Palladium on γ-Alumina by X-Ray Photoelectron. Appl. Catal., B 1992, 1, 1−12. (c) Deshpande, P. A.; Hegde, M. S.; Madras, G. Pd and Pt Ions as Highly Active Sites for the Water-Gas Shift Reaction over Combustion Synthesized Zirconia and Zirconia-Modified Ceria. Appl. Catal., B 2010, 96, 83−93.

(23) (a) Kim, K. S.; Gossmann, A. F.; Winograd, N. X-Ray Photoelectron Spectroscopic Studies of Palladium Oxides and the Palladium-Oxygen Electrode. Anal. Chem. 1974, 46, 197−200. (b) Kim, D. H.; Woo, S. I.; Lee, J. M.; Yang, O. B. The Role of

Lanthanum Oxide on Pd-Only Three-Way Catalysts Prepared by Co-Impregnation and Sequential Impregnation Methods. Catal. Lett. 2000, 70, 35−41. (c) Kibis, L. S.; Titkov, A. I.; Stadnichenko, A. I.; Koscheev, S. V.; Boronin, A. I. X-Ray Photoelectron Spectroscopy Study of Pd Oxidation by RF Discharge in Oxygen. Appl. Surf. Sci. 2009, 255, 9248−9254.

(24) Zhu, X. L.; Liu, S. B.; Man, B. Y.; Xie, C. Q.; Chen, D. P.; Wang, D. Q.; Ye, T. C.; Liu, M. Analysis by Using X-Ray Photoelectron Spectroscopy for Polymethyl Methacrylate and polytetrafluoroethylene Etched by KrF Excimer Laser. Appl. Surf. Sci. 2007, 253, 3122−3126.

(25) Stocco, A.; Drenckhan, W.; Rio, E.; Langevin, D.; Binks, B. P. Particle-Stabilised Foams: an Interfacial Study. Soft Matter 2009, 5, 2215−2222.

(26) Surface tension values of some common test liquids for surface energy analysis; http://www.surface-tension.de/ (accessed 2021-05-26).

(27) Watts, H. D.; Mohamed, M. N. A.; Kubicki, J. D. Evaluation of Potential Reaction Mechanisms Leading to the Formation of Coniferyl Alcohol α-Linkages in Lignin: a Density Functional Theory Study. Phys. Chem. Chem. Phys. 2011, 13, 20974−20985.